Broadband attenuation of Lamb waves through a periodic array of thin rectangular junctions

Rayisa P. Moiseyenko, Yan Pennec, Rémi Marchal, Bernard Bonello, Bahram Djafari-Rouhani

Broadband attenuation of Lamb waves through a periodic array of thin rectangular junctions

Rayisa P. Moiseyenko,[1,2] Yan Pennec,[1,2] Rémi Marchal,[3,4] Bernard Bonello,[3,4] and Bahram Djafari-Rouhani[1,2]
[1]*Institut d'Electronique, de Microélectronique et de Nanotechnologie (IEMN-UMR CNRS 8520), Villeneuve d'Ascq, France*
[2]*Université Lille1, UFR de Physique, Cité Scientifique, 59652 Villeneuve d'Ascq Cedex, France*
[3]*Institut des NanoSciences de Paris (INSP-UMR CNRS 7588), Paris, France*
[4]*Université Pierre et Marie Curie (box 840) 4, place Jussieu, 75252 Paris Cedex 05, France*
(Received 22 March 2014; revised manuscript received 11 September 2014; published 15 October 2014)

We study theoretically subwavelength physical phenomena, such as resonant transmission and broadband sound shielding for Lamb waves propagating in an acoustic metamaterial made of a thin plate drilled with one or two row(s) of rectangular holes. The resonances and antiresonances of periodically arranged rectangular junctions separated by holes are investigated as a function of the geometrical parameters of the junctions. With one and two row(s) of holes, high frequency specific features in the transmission coefficient are explained in terms of a coupling of incident waves with both Fabry-Perot oscillations inside the junctions and induced surface acoustic waves between the homogeneous part of the plate and the row of holes. With two rows of holes, low frequency peaks and dips appear in the transmission spectrum. The choice of the distance between the two rows of holes allows the realization of a broadband low frequency acoustic shielding with attenuation over 99% for symmetric waves in a wide low frequency range and over 90% for antisymmetric ones. The origin of the transmission gap is discussed in terms of localized modes of the "H" element made by the junctions, connecting the two homogeneous parts of the plate.

DOI: 10.1103/PhysRevB.90.134307 PACS number(s): 43.20.+g, 43.35.+d, 62.30.+d

I. INTRODUCTION

Artificial structures with special sound properties not found in ordinary materials have been a hot topic during the last twenty years. The well-known phononic crystals (PCs) [1,2], defined as periodic structures, are composed of at least two contrasted materials for the inclusions and the matrix. They have first attracted attention due to the possibility of creating a band gap in the Bragg frequency regions, where the acoustic waves are forbidden whatever the direction of propagation. Many applications have been studied, around the manipulation of the acoustic waves, such as guiding, filtering, demultiplexing [3] as well as negative refraction properties, focusing, self-collimation, and beam splitting [4]. More recently, a novel class of materials appears where the size of the inclusions is much smaller than the driving wavelength [5,6]. During the last few years many works report on low frequency band gaps in acoustic slabs, mainly using pillars [7–9], double side symmetric pillars [10], or stepped pillars [11]. Acoustic wave transmission has been also investigated in one-dimensional (1D) acoustic gratings with subwavelength junctions [12–15] or two-dimensional (2D) panels periodically perforated with holes [16,17], then on double fishnet structures [18]. These acoustic metamaterials are used to reach unusual physical properties, such as acoustic induced transparency or enhanced acoustic transmission [19–23] as well as sound shielding [24–27].

The mechanisms responsible for these specific properties found their origin from multiple interferences combining local resonances and antiresonances, Fabry-Perot oscillations [12,18,28] and induced acoustic surface waves, nonleaky surface waves [29,30]. While most of the aforementioned works studied solid inclusions in a fluid as the host material, the reverse situation, i.e., solid as host and fluid as inclusion, is less considered [31].

In this work, we present the study of analogous phenomena for a Lamb waves propagating in a thin silicon plate drilled with one or two lines of rectangular air holes. The full Lamb waves, i.e., symmetric S_0 and antisymmetric A_0, have been treated with an emphasis of the symmetric ones in our discussions and results. In this work, we choose rectangular holes due to the fact that more geometrical parameters, i.e., the length and width, respectively, can be controlled comparated to circular holes. In particular, the occurrence of frequency dips and peaks in the transmission spectrum are discussed and optimized for the purpose of sound attenuation. We show that the propagation of sound through two layers of junctions separating rectangular holes conserve several features arising from one row and at the same time new features proper to two rows appear. Therefore, we demonstrate the design of an acoustic metamaterial slab displaying a broadband low frequency sound shield for symmetric acoustic and antisymmetric Lamb waves. The denomination of "metamaterial" is used in this latter case because the transmission band gap appears at large wavelengths (low frequencies) as compared to the geometrical parameters of the structure. Such study can be useful for microelectromechanical system (MEMS) structures where solid plates are considered as incident medium and where particular parts should be preserved at certain frequency ranges.

The paper is organized as follows. In Sec. II, we consider the case of a periodic array of one row of junctions separated by holes and discuss the effects of the geometrical parameters on the features appearing in the transmission spectrum. In Sec. III, we consider the case of two rows of holes and especially investigate the possibility of broadband shielding by an appropriate choice of the distance between the two rows. The relationship between the transmission curves and the dispersion ones is then analyzed in Sec. IV. Finally, conclusions and perspectives are drawn in the last section.

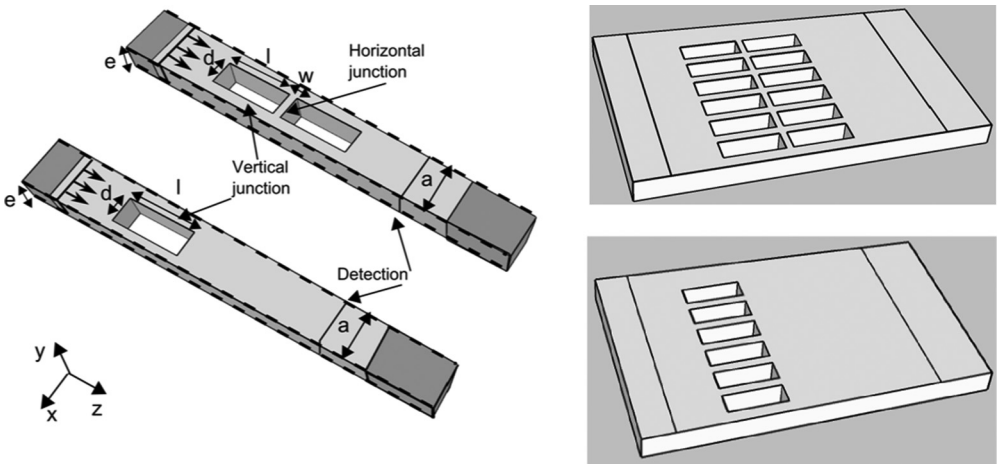

FIG. 1. Schematic view of the unit cell of the acoustic metamaterial silicon slab of thickness e drilled with one or two rows of rectangular holes of width d and length l. The lattice parameter is a and the distance between the two holes is w. Periodic boundary conditions are applied to each side of the unit cell, in the direction x while perfect matching layers (dark gray areas) are applied in the direction of propagation z. The input symmetric Lamb wave S_0 is launched from the left side of the structure.

II. GEOMETRY AND TRANSMISSION SPECTRA

Figure 1 represents a schematic view of the unit cell used for the calculation of the transmission through one and two rows of rectangular junctions separated by air holes drilled in a silicon plate. The geometrical parameters involved in the structure are the lattice parameter $a = 1$ mm, taken as the length unit for the definition of the other parameters, the width d and the length l of the rectangular hole, the thickness of the plate e, and the distance w between the two rows of holes. The thickness of the plate e has been taken equal to $0.5a$ in all the following simulations. Additional calculations with different plate thicknesses from $0.1a$ to $0.5a$ yield similar features and will not be presented here. The silicon is taken as a cubic material with the elastic constants $C_{11} = 165.7$ GPa, $C_{12} = 63.9$ GPa, and $C_{44} = 79.62$ GPa and mass density $\rho = 2331$ kg/m^3.

We calculate the transmission of incident Lamb waves along the direction of propagation z. As the modes in the structure can be distinguished as symmetric or antisymmetric with respect to the middle plane of the plate, the calculations of the transmission spectra have been performed separately. For the features presented in this paper and especially the finding of a broadband attenuation band, we mainly concentrate on the symmetric modes, while discussing briefly the case of antisymmetric modes. As will be shown later, the reason is the diffraction phenomena related to the folding of the A_0 branch of the plate that occurs at a frequency about two times smaller than for the S_0 branch, therefore blurring some of the physical effects of interest in this paper. All transmission computations have been performed using a finite difference time-domain method (FDTD) [31]. Periodic boundary conditions are applied on each side of the unit cell in the x direction and, as the unit cell is finite along z, perfect matching layers (PML) are applied on the left and right sides of the structure (dark gray regions) to avoid any reflections coming back from the external boundaries. The incident wave S_0 (resp. A_0) propagating in the z direction is launched by applying a harmonic displacement u_z (resp. u_y) in an (x,y) plane situated in front of the holes. The detection of the displacement field is done after the holes, at the right side of the structure. The far field transmission T is defined as the ratio between the average amplitude of the components of displacement u_k, $k \in \{x,y,z\}$, along half of the phononic plate section and the modulus of the displacement field u_{ref} through the perfect plate. In the following, the transmission is presented either with a linear scale $T_k = u_k/u_{\text{ref}}$ or with a logarithmic one, T_k (dB) $= 10\log_{10}(u_k/u_{\text{ref}})$.

It should be noticed that in the computation of the transmission coefficient by the FDTD method, the resolution of the sharp peaks and dips, especially as concerns their amplitudes, may need a large number of time steps and even very fine meshes in the real space. This may become a very time consuming process when it needs to be repeated for several sets of geometrical parameters. Therefore, when the physical origin of the behaviors is well understood, we make a compromise between the time of calculation and the resolution of the peaks.

A. Transmission through one row of rectangular holes

We first describe and discuss in details the propagation of the symmetric Lamb waves S_0 through one row of rectangular holes. The main features in the transmission spectra that will be discussed below are related to the Fabry-Perot resonances inside the thin junctions, the resonances associated with the localized (interface) modes at the boundaries of the row of junctions with the homogeneous parts of the plate on both sides, and the interaction between both types of resonances. In particular, the excitation of the interface modes gives rise to a zero in the transmission spectra and when a Fabry-Perot resonant peak approaches this zero, it becomes very sharp and displays a Fano profile.

A typical transmission curve is presented Fig. 2(a) for the holes parameters $d = 0.9a$ and $l = 0.4a$ and for each component of the displacement field, i.e., u_x (green), u_y (red), and u_z (black). One can notice the occurrence of three specific features, namely, two peaks P_1 and P_2 surrounding one zero

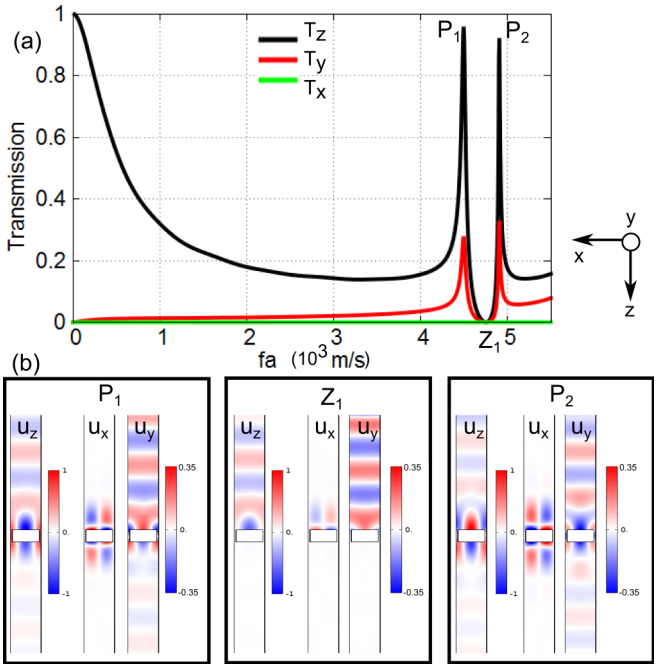

FIG. 2. (Color online) (a) Transmission coefficients calculation as a function of the reduced frequency for the three components u_x (green), u_y (red), and u_z (black) of the symmetric Lamb wave S_0 through one row of rectangular holes for the geometrical parameters: $d = 0.9a, l = 0.4a$. (b) Cartography of the displacement fields for the three components at the frequencies of the two peaks P_1 (left) and P_2 (right) and the dip Z_1 (center). The red (blue color) corresponds to a positive (negative) displacement with a zero represented with the white color. For the components u_x and u_y the color bar has been magnified for a better observation of the field.

of transmission, Z_1. Figure 2(b) gives the three components of the displacement field (transverse u_x, longitudinal u_y, and perpendicular u_z) at the respective monochromatic frequencies of the dip Z_1 and the peaks P_1 and P_2. Due to the fact that the two components u_x and u_y are almost three times lower than the component u_z, the color scales have been chosen differently for each component. From Fig. 2(b) at the frequency of the zero of transmission, Z_1 is associated with an excitation of a mode at the interface between the homogeneous incident medium and the periodic row of rectangular holes. One can notice an enhancement of the field in the vicinity of the surface whereas the wave does not penetrate inside the junctions. Such an excitation can be explained by the fact that the normal incident wave with a wave vector $k_{//}$ (parallel to the interfaces) equal to zero can be coupled to modes having a wave vector equal to a reciprocal lattice vector, namely, $m(2\pi/a)$ where m is an integer. The zero of transmission Z_1 is associated with an excitation of geometrically induced acoustic surface waves issued from multiple interferences at a wavelength closed to the grating pitch, sometimes called Wood's anomalies [32,33]. Close to the zero of transmission, from each side of the dip, two peaks P_1 and P_2 occur for which the displacements fields are respectively represented in Fig. 2(b). One can clearly see an enhancement of the acoustic wave inside the vertical junctions and at the interfaces between both homogeneous media and the array of rectangular holes. Therefore, the two peaks correspond to a coherent coupling between the diffracted waves excited on interfaces and the Fabry-Perot resonant modes inside the junctions. The difference between the two peaks comes from the symmetry of the mode which is respectively antisymmetric for P_1 and symmetric for P_2 with respect to the middle plane of the junction, perpendicular to the slab.

Let us notice that the far field transmitted wave is very similar to the S_0 Lamb mode of the incident wave, although with a different amplitude. In particular, the displacement field is mainly longitudinal with a ratio between the components u_z and u_y in agreement with its analytical expression [34] whereas the component u_x does not show up. This means that the transmission through the layer of junctions did not give rise to any mode conversion in the considered frequency range, although the near field displacement field becomes quite different from the Lamb mode.

Figure 3 shows the evolution of the transmission curve with respect to the main component u_z as a function of the length l of the junction for $d = 0.9a$. Increasing l from $0.1a$ to $2a$ allows more Fabry-Perot resonances inside the length of the thin junctions P_1, P_2, P_3, and P_4; thus the resonance frequencies move towards lower frequencies. In particular, when one of the resonant peaks approaches the zero of transmission from above, it becomes very narrow and sharp, then crosses the zero for a slightly bigger length of the junctions, and finally broadens when going to lower frequencies. In the latter case, the origin of the peak becomes again a Fabry-Perot resonance without any interaction with the interface modes. At the beginning of Sec. II, amplitudes of the sharp transmission peaks near the dip can be increased and reach unity by increasing the number of the time steps or by using a finer mesh in the FDTD computations. So, the fact their values remain well below 1 is related to the computation and not to a physical mechanism.

The evolution of the features (in particular, P_1, P_2, and Z_1) as a function of the geometrical parameters of the rectangular hole is summarized in Figs. 4(a) and 4(b). In these diagrams, the transmission is represented in linear scale ($T = u_z/u_{\text{ref}}$) with a color bar where the yellow (resp. black) color corresponds to a high (resp. low) transmission coefficient. Figure 4(a) shows the evolution of the transmission as a function of the width d, for a constant length $l = 0.4a$. One can see that, for a given length, the frequencies of P_1, Z_1, and P_2 are only slightly dependent upon the width of the silicon junctions as far as the latter remain thin ($d > 0.4a$). The attenuation at low frequencies ($fa < 4000$ m/s) can reach 80% when the values of d are higher than $0.8a$ [purple area in Fig. 4(a)]. Figure 4(b) summarizes the evolution of the transmission as a function of the length, keeping $d = 0.9a$. One can see that the dip Z_1 which corresponds to the lower level of transmission (black color) is almost not affected by changing the length of the junctions. We also clearly see the position of the Fabry-Perot maxima which shift to the low frequencies when l increases. It is again worth noticing the fast variation of the Fabry-Perot modes as a function of l when they are far from the interface modes and their flattening when they approach the zero of transmission and interact with the interface modes. Finally one can note that the level of transmission at low frequency ($fa < 4000$ m/s) is almost kept constant as a function of l, leading to an attenuation coefficient

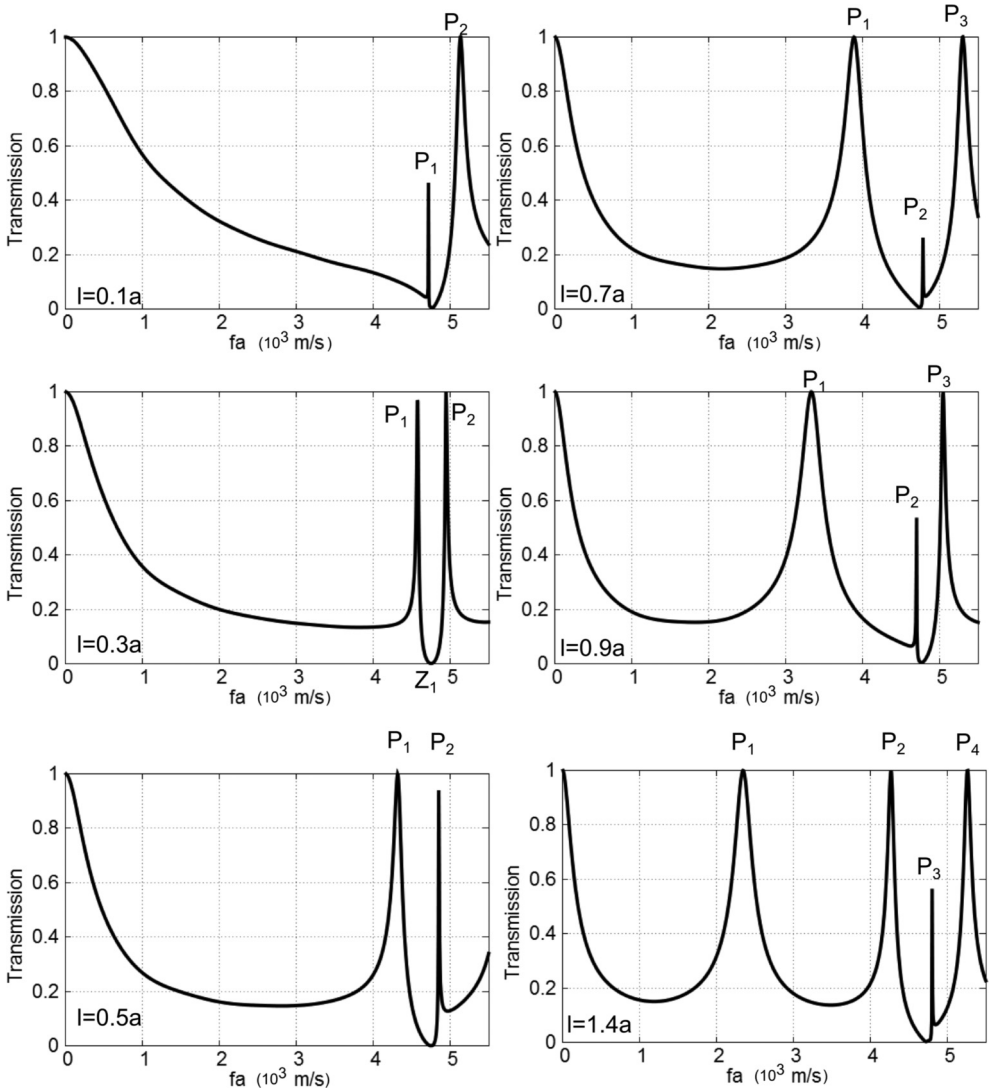

FIG. 3. Evolution of the transmission curve for the symmetric Lamb wave S_0 with respect to the main component u_z as a function of the length l of the hole, with $d = 0.9a$. P_i, where i is an integer, represents the positions of the Fabry-Perot maxima inside the vertical junction.

in the range of 80% (purple area) related to a minimum of the Fabry-Perot oscillations between two maxima.

Similarly to the case of symmetrical modes, we have calculated the incident A_0 wave transmission launched through the layer of holes. However, the study of the A_0 mode will be limited to a more restricted frequency range ($fa < 4000$ m/s) to avoid the folded A_0 mode in the first Brillouin zone reaching the wave vector $k_x = 0$. Above 4000 m/s, the transmission curve leads to diffraction phenomena, almost independently of the thickness of the plate which blur the physical effects. Figure 5 gives the transmission spectra coefficient for the A_0 mode for different values of the length l ($0.4a$, $0.8a$, and $1.2a$) while keeping constant the width $d = 0.9a$. Qualitatively, the behavior of the transmission is similar to what has been observed previously in the S_0 case. Just before $fa = 4000$ m/s, the transmission curve presents a narrow peak followed by a dip which both have the same origin as described previously for the S_0 wave. When increasing the length l to $0.8a$ then $1.2a$, one can see that the peak shifts to the low frequencies while a new one appears in the vicinity of the dip ($l = 0.8a$). The results of the calculation are summarized in the bottom right panel where the transmission is represented with a color scale in a frequency versus length figure. We can see the similar trend for Fabry-Perot resonances as for S_0, namely, an increasing number of peaks at low frequency which become closer to each other as far as l increases with a constant dip in the vicinity of $fa = 4000$ m/s (black color in the graph).

B. Transmission through two rows of rectangular holes

We now turn to the investigation of the propagation of the symmetric Lamb waves S_0 through two rows of rectangular junctions, especially for the purpose of a low frequency broadband acoustic shielding. Based on the previous discussions for the case of symmetric Lamb waves S_0, the width of the holes is chosen to be $d = 0.9a$ that insures a low level of transmission and the length to $l = 0.4a$ to avoid all Fabry-Perot maxima in the low frequency range. Then, we investigate the behavior of the transmission as a function of the distance w between the two rows of junctions (see the schematic view of Fig. 1).

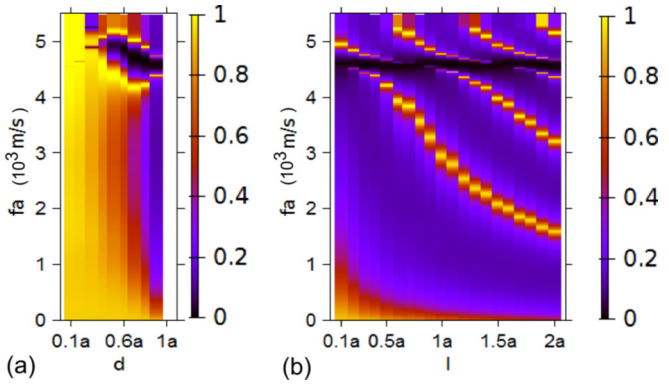

FIG. 4. (Color online) Evolution of the transmission coefficient for the symmetric Lamb wave S_0 with respect to the main component u_z as a function of (a) the width d when $l = 0.4a$ and (b) the length l when $d = 0.9a$. The yellow (resp. black) color corresponds to the high (resp. low) transmission coefficient represented in scalar scale.

Figure 6(a) presents a typical transmission curve for a distance of $w = 0.4a$ for all components of the displacement field u_x, u_y, and u_z. Again, the component u_x doesn't show up in far field. For the two other components, one can observe several peaks and dips which are new as compared to the transmission through one row of holes, especially at low frequencies. Let us notice again that, in the far field the vibration becomes similar to the S_0 Lamb mode and does not show any mode conversion in the considered frequency range. The distribution of the displacement fields for each peak and dip is reported in Fig. 6(b). At high frequency ($fa > 4000$ m/s) we find a zero of transmission Z_1', which has almost the same frequency and displacement field as the dip Z_1 described in the previous section for one row of holes. The origin is the same and comes from an excitation of the mode at the interface between the homogeneous incident medium and the periodic structure. Close to the dip, we also find a peak labeled P_1' with the same characteristics than the previous peaks P_1 and P_2, except that now the induced interface waves are localized on both sides of the double layer element, in contact with the homogeneous media.

At lower frequencies ($fa < 4000$ m/s), new features labeled Z_2', P_2', and P_3' can be observed that do not exist in the case of one monolayer of rectangular holes. The displacement field calculations for these three features at their respective frequencies show an enhancement of the acoustic field inside the horizontal junction separating the two rows of rectangular holes.

The origin of the two peaks and the dip is discussed in relation with the resonance characteristics of the "H" element presented in Fig. 7(a). For this purpose, we calculate using a finite element method [35] the eigenmodes of the H element constituting the vertical and horizontal junctions when the upper and bottom faces shown with hatched area in Fig. 7(a) are clamped while the other surfaces are left free of stress. Under these conditions, the following five eigenmodes for the H element in the considered frequency range. We found the symmetric fundamental mode S_1 and a higher order mode S_3 at the respective frequencies of 1580 and 3530 m/s [Fig. 7 (b)]. One can clearly make the link between the elastic distribution obtained for the peak P_2' (resp. P_3') and the mode S_1 (resp. S_3).

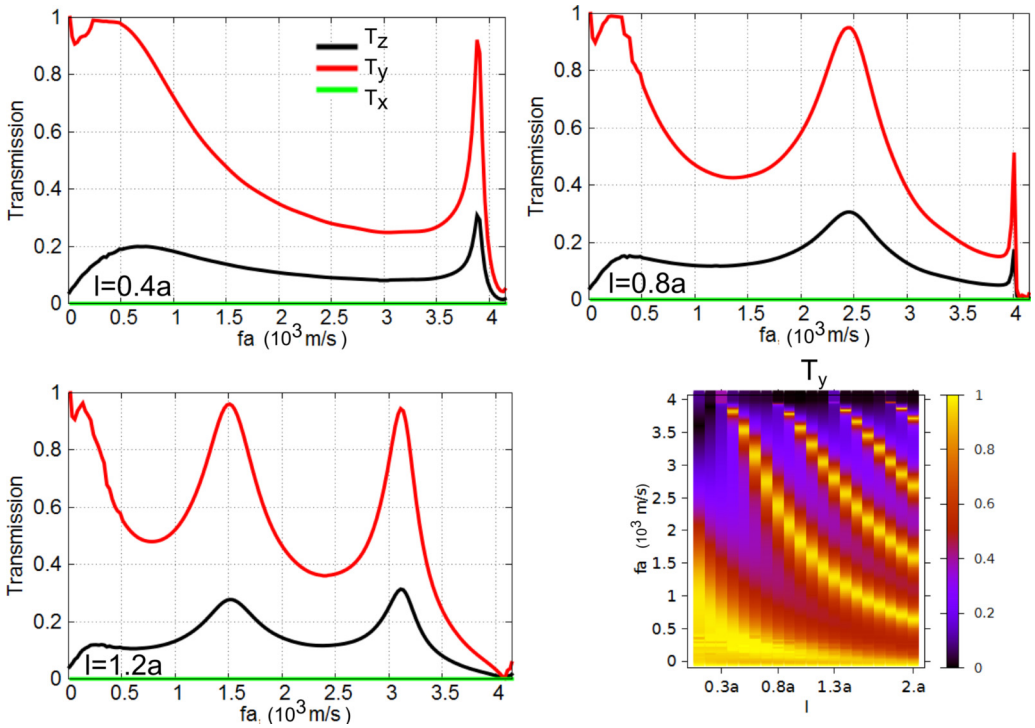

FIG. 5. (Color online) Evolution of the transmission curve for the three components u_x (green), u_y (red), and u_z (black) of the antisymmetric Lamb wave A_0 with $d = 0.9a$ and for three values of the length l of the holes. Bottom right panel: Evolution of the transmission coefficient T_y of the A_0 mode as a function of the length l when $d = 0.9a$. The yellow (resp. black) color corresponds to the high (resp. low) transmission coefficient represented in scalar scale.

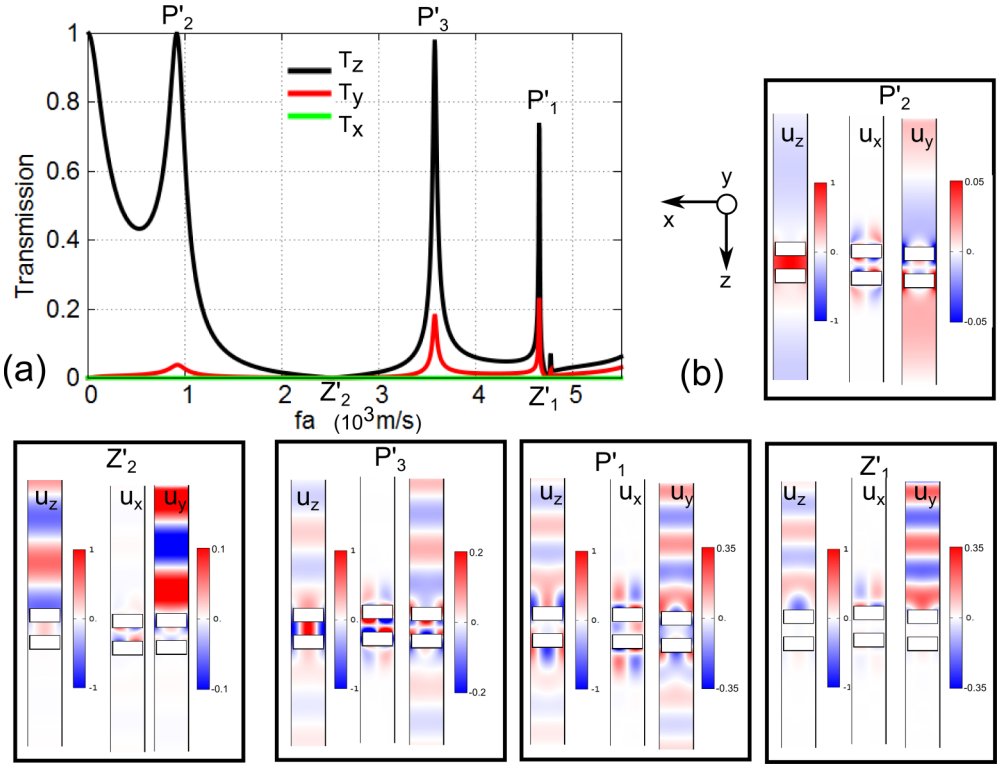

FIG. 6. (Color online) (a) Transmission coefficients for each component calculated as a function of the reduced frequency for the three components u_x (green), u_y (red), and u_z (black) of the symmetric Lamb wave S_0 through two rows of rectangular holes for the geometrical parameters: $d = 0.9a$, $l = 0.4a$, and $w = 0.4a$ (b) Transversal, perpendicular, and longitudinal components u_x, u_y, and u_z, respectively, of the displacement fields at the frequencies of the three peaks P_1', P_2', and P_3' and the two dips Z_1' and Z_2'. The red (blue color) corresponds to a positive (negative) displacement while the white color represents the zero. For the components u_x and u_y the color bars have been chosen differently to magnify the corresponding field.

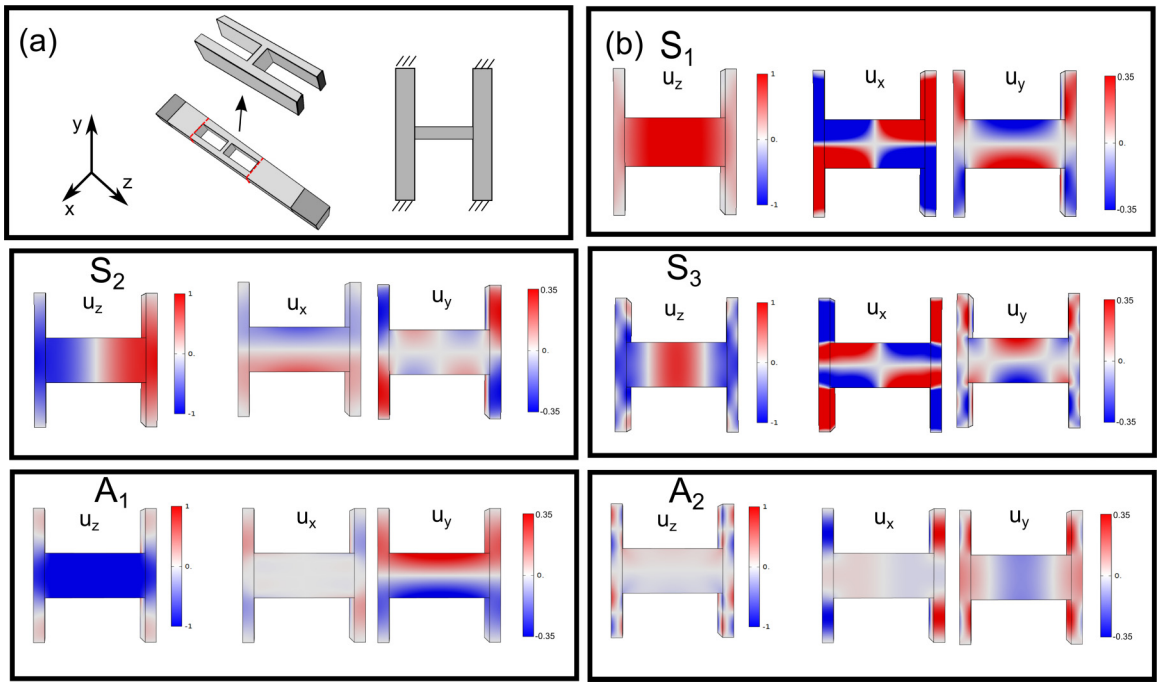

FIG. 7. (Color online) (a) Definition of an H element extracted from the periodic unit cell. (b) Useful symmetric eigenmodes of the H element at 1580 (S_1), 2840 (S_2), and 3530 m/s (S_3) and antisymmetric at 1820 (A_1) and 3840 m/s (A_2) with fixed boundaries condition applied on each vertical junction [hatched area in (a)]. The symmetric mode S_2 is also an eigenmode of the H element but cannot be excited by the incident wave since it is antisymmetric with respect to the z axis. The red (blue color) corresponds to a positive (negative) displacement with a zero represented with the white color.

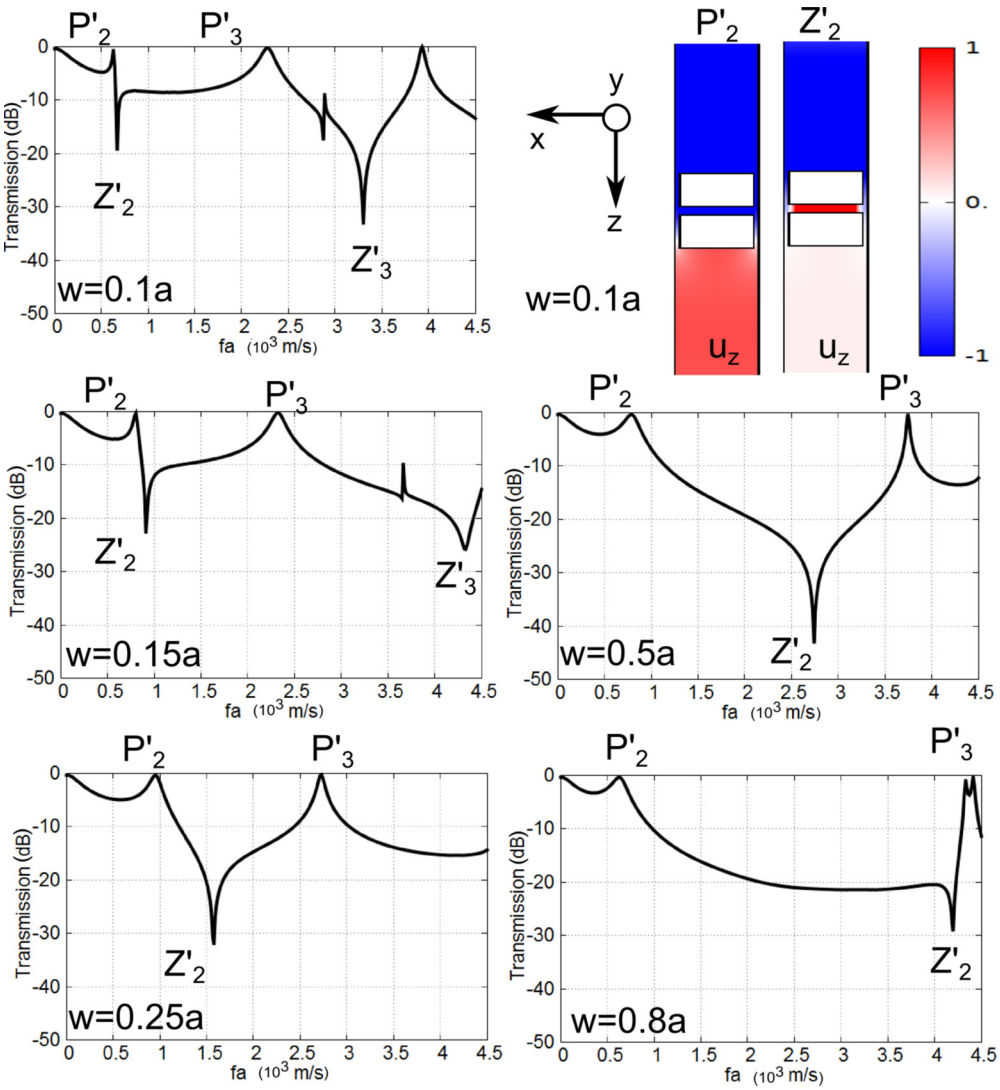

FIG. 8. (Color online) Evolution of the transmission coefficient of the symmetric Lamb wave S_0 with respect to the main component u_z at low frequency ($fa < 4500$ m/s) as a function of the width w between the two rows of rectangular holes for $l = 0.4a$. Upper right panel: Displacement field distributions at the frequency of the peak (left) and the dip (right) for $w = 0.1a$; the red (blue color) corresponds to a positive (negative) displacement with a zero represented with the white color.

It is worth noticing that the mode S_2 (2840 m/s) is also an eigenmode of the H element which is symmetric with respect to the middle plane of the plate. However, it is antisymmetric with respect to the z axis and cannot be excited by an incident S_0 mode. Then we also obtain an antisymmetric modes A_1 and A_2 (with respect to the middle plane of the plate) at 1820 and 3840 m/s, respectively, that will be discussed when A_0 excitation is considered.

To understand the origin of the zero Z_2', we have represented in Fig. 8 the evolution of the three low frequency features with respect to the main component u_z as a function of the distance w between the two rows of holes for a constant $l = 0.4a$. To emphasis the position and deepness of the zero of transmission Z_2', the transmission coefficient is shown with a logarithmic scale.

When $w = 0.1a$, one can see that the peak P_2' and the dip Z_2' belong to a lone asymmetric shaped peak known as a Fano-like resonance for which the upper right panel in Fig. 8 shows the respective displacement field distributions. At the frequency of the peak (left), the horizontal bar vibrates in phase with the incident wave and leads to a maximum of transmission (in red color). On the contrary, at the frequency of the dip (right), the horizontal H bar vibrates in the opposite phase with the incoming wave and leads to a zero of transmission (in white color). The origin of the resonance comes from the mode S_1 of the H element which leads to a transmitted peak P_2' and a zero of transmission Z_2' depending on whether the incident wave is out of phase or in phase with the resonance of the localized mode S_1. Mode S_3 gives also rise to a pair of peak P_3' and dip Z_3' which can be seen for $w = 0.1a$ and $w = 0.15a$. When w increases, the zero of transmission Z_2' is shifted toward the higher frequencies and the distribution of its elastic field progressively changes from the P_2' shape to the P_3' appearance. For large values of w ($w > 0.5a$), a large and deep low frequency band gap is then obtained, with the edges delimited with the peaks P_2' and P_3'.

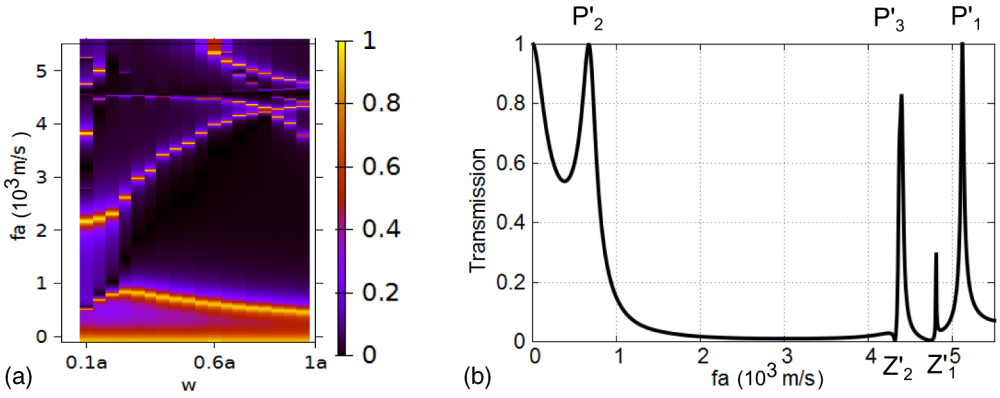

FIG. 9. (Color online) (a) Evolution of the transmission coefficient of the symmetric Lamb wave S_0 with respect to the main component u_z as a function of the distance w between the two rows of rectangular holes: the yellow (resp. dark blue) color corresponds to the high (resp. low) coefficient. (b) Highlight of the widest low frequency band gap for the optimized set of parameters: $d = 0.9a$, $l = 0.4a$, and $w = 0.8a$: the attenuation reaches 99% of the input signal.

The evolution of these peaks and dips as a function of the distance w between the two rows is reported in Fig. 9(a). In this diagram, the transmission is represented in a linear scale ($T = u_z/u_{\text{ref}}$) with a color bar where the yellow (resp. black) color corresponds to a high (resp. low) transmission coefficient. The peak and dip pair (P_1',Z_1') is almost not affected by the variation of the distance w between the two holes while the peak P_2' slowly decreases. The positions of the peak P_3' and the dip Z_2', on the contrary, shift to the high frequencies when the distance w increases. This behavior opens the way to an optimization of the width of the low frequency band gap for $w = 0.8a$. The corresponding transmission curve is shown on Fig. 9(b) and displays a broadband sound attenuation at low frequency, over 95% between the frequencies 1070 and 4270 m/s and even over 99% between 2010 and 4240 m/s, finally of 99.9% in the dip Z_2'. It should be noted that the lowest edge of the band gap reached $fa = 1000$ m/s, that corresponds to a wavelength more than 5 times the lattice parameter ($a/\lambda = 0.17$ for a silicon transverse velocity of 5844 m/s).

Then, we have also investigated the evolution of the three features with respect to the main component u_z as a function of the length of the vertical junctions, keeping $w = 0.8a$ and $d = 0.9a$ (Fig. 10). When increasing the length of the holes, we introduce Fabry-Perot resonances inside the vertical junctions which progressively shift to the lower frequencies. Indeed, the variation of the length offer the opportunity to tune selective sharp transmission peaks inside the low frequency gap then offering possibilities of filtering and sensing applications.

Similar behavior can be obtained with the antisymmetric excitation of the structure. Figure 11(a) represents a typical transmission curve when the antisymmetric Lamb wave A_0

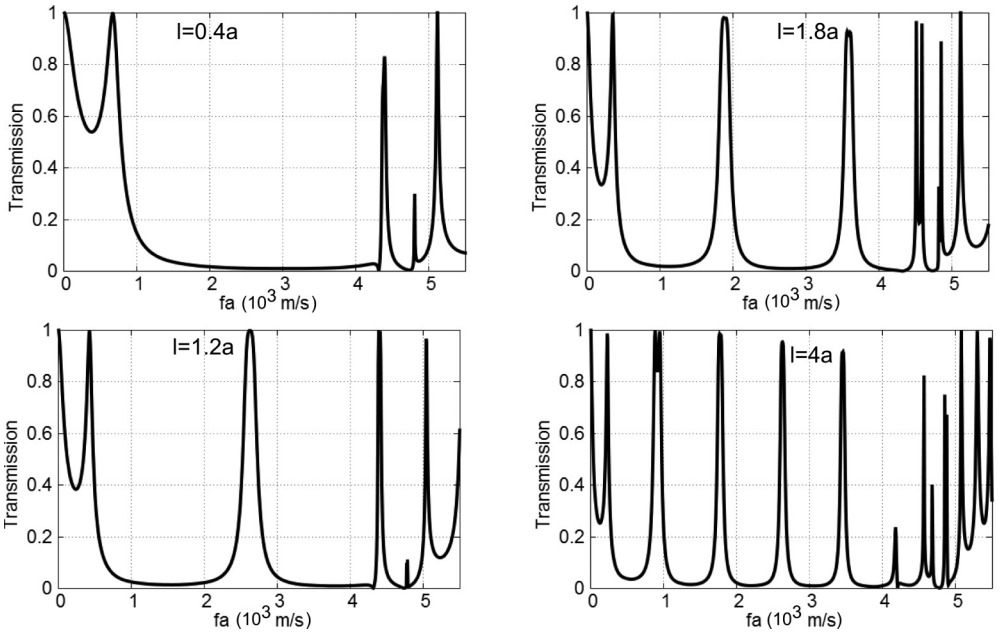

FIG. 10. Evolution of the transmission coefficient for the S_0 mode with respect to the main component u_z as a function of the length of the holes when $w = 0.8a$ and $d = 0.9a$.

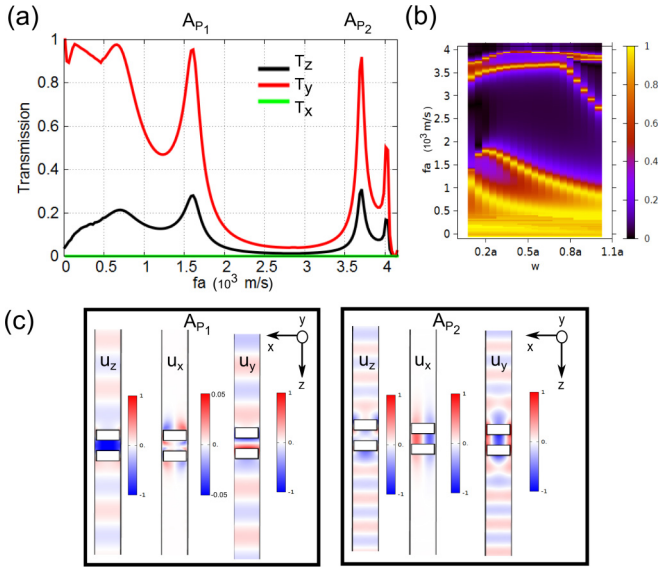

FIG. 11. (Color online) (a) Transmission coefficient of the A_0 mode for $w = 0.4a$. (b) Evolution of the transmission coefficient for the A_0 mode with respect to the main component u_y as a function of the distance w between the two rows of rectangular holes: the yellow (resp. dark blue) color corresponds to the high (resp. low) coefficient. (c) u_x, u_y, and u_z displacement fields at A_{P_1} and A_{P_2} for $w = 0.4a$.

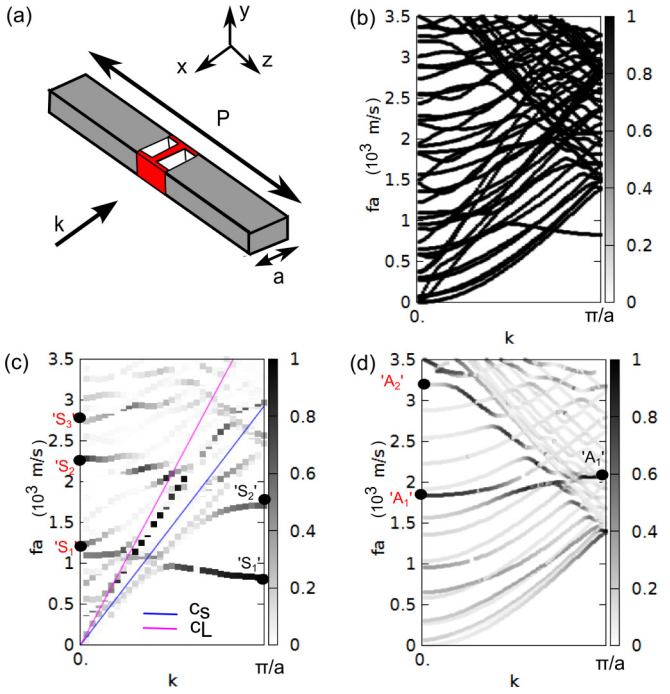

FIG. 12. (Color online) (a) Unit cell for the band structure calculation with periodic boundaries conditions applied in the x and y directions. (b) Band structure calculated in the direction parallel to the holes lines for $w = 0.2a$. Band sorting calculation for $P = 9a$, $d = 0.9a$, $l = 0.4a$, and $w = 0.2a$, selecting the modes (c) symmetric and (d) antisymmetric with respect to the middle plane of the plate. The grayscale color bar defines the amount of displacement of the eigenmodes concentrated in the H element with respect to the displacement field in the whole unit cell.

is considered. One can see the occurrence of new peaks A_{P_1} and A_{P_2} which lead to the opening of a large band gap at low frequencies. Figure 11(b) reports in a color map the evolution of the transmission as a function of the frequency and the distance w between the two rows. In this diagram, the transmission is represented in a linear scale ($T = \sqrt{(u_z^2 + u_y^2)}/u_{\text{ref}}$) with a color bar where the yellow (resp. dark blue) color corresponds to a high (resp. low) transmission coefficient. The peak A_{P_2} is almost not affected by the variation of the distance w between the two holes while the peak A_{P_1} slowly decreases. In parallel, when the distance w increases, Fabry-Perot resonances appear progressively at low frequencies as discussed previously ($w > 0.7a$). This behavior opens the way to an optimization of the distance w between the two rows in the goal to obtain a large band gap at low frequency. The smaller band gap has been obtained for the same value ($w = 0.8a$) than for the S_0 incident wave [Fig. 9(a)] displaying a broadband sound attenuation at low frequency of 80% between the frequencies 1800 and 3500 m/s and over 90% between the frequencies 2100 and 3200 m/s. The origin of the two peaks is associated to the resonance of the H element presented in Fig. 7. We found that the antisymmetric fundamental mode A_1 and a higher order mode A_2 at the respective frequencies of 1820 and 3840 m/s present the same distribution of the elastic field at the same frequencies than the peaks A_{P_1} and A_{P_2} [Fig. 11(c)].

III. DISPERSION CURVES OF TWO LAYERS OF RECTANGULAR HOLES

The object of this section is to give the relationship between the features in the transmission coefficient discussed in the previous section and the dispersion curves of the structure consisting of the two rows of holes. Indeed, this is a periodic system along x for which the dispersion curves can be represented as a function of the wave vector parallel to the x axis in a reduced one-dimensional Brillouin zone. The method of calculation consists of making the structure superperiodic along the z direction by repeating periodically the two rows of holes along z, with a period P much larger than the physical period a [Fig. 12(a)]. Another method (not presented here) would consist of considering a finite plate of large length L along z and put the two rows of holes in the middle. In both cases, many dispersion branches are obtained whose number increases with the size of the superperiod P or the length L because the amount of matter increases with P or L. Two examples are shown in Figs. 12 and 13 where $P = 9a$, $d = 0.9a$, $l = 0.4a$, and $w = 0.2a$ or $w = 0.4a$. The first case of $w = 0.2a$ is introduced in order to show well defined resonance modes (flat branches). However $w = 0.4a$ can be directly used for comparison with transmission shown in Fig. 6. Figure 12(b) represents the full dispersion curve when $w = 0.2a$. The separations of the dispersion curves into symmetric and antisymmetric modes with respect to the middle plane of the plate are given in Figs. 12(c) and 12(d). It is worth mentioning that these modes are propagative (leaky) as long as they fall above the sound line (given as reference below transverse and longitudinal

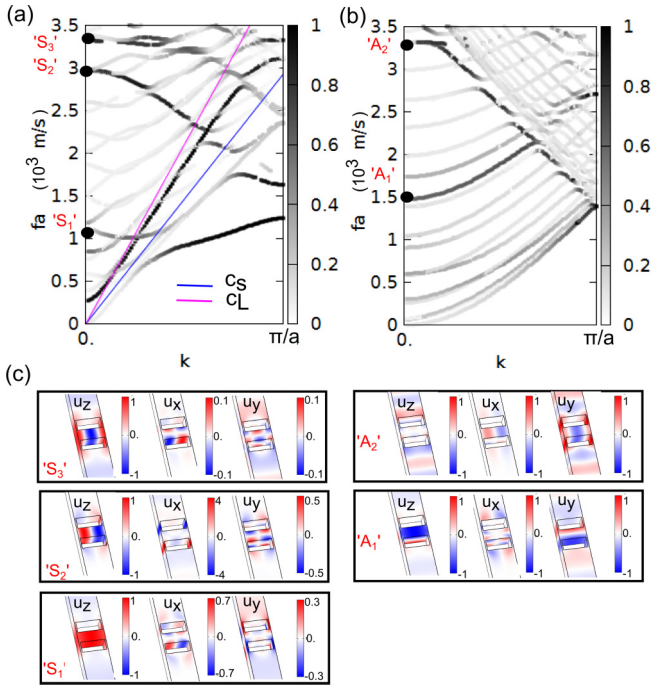

FIG. 13. (Color online) Band sorting calculation for $P = 9a, d = 0.9a$, $l = 0.4a$, and $w = 0.4a$, selecting the modes (a) symmetric and (b) antisymmetric with respect to the middle plane of the plate. The grayscale color bar defines the amount of displacement of the eigenmodes concentrated in the H element with respect to the displacement field in the whole unit cell. (c) Transversal, perpendicular, and longitudinal components u_x, u_y, and u_z of the displacement fields at the frequencies of the two modes S_1, S_2, S_3 and A_1, A_2 indicated with red font in (a) and (b). The red (blue) color corresponds to a positive (negative) displacement while the white color represents the zero. For the components u_x and u_y the color bars have been chosen differently from time to time to magnify the corresponding field.

velocities in silicon $c_S = 5900$ and $c_L = 8400$ m/s) of the plate whereas they become localized around the holes (nonleaky) only when they are situated below the sound line. Nevertheless, even in the leaky region, the branches which are induced by the presence of the holes should display a sufficient localization in their close vicinity. This means that they can be identified by a band sorting method. The latter consists of representing with a light or saturated color the amount of energy concentrated around the holes [Fig. 12 (a)]. Namely for the symmetric branches where the main component of the displacement is u_z, the color on the curves is defined by the quantity $\int_{V_H} |u_z|^2 dV / \int_{V_{\text{unitcell}}} |u_z|^2 dV$. Similarly, for the antisymmetric branches the band sorting is based on the quantity $\int_{V_H} (|u_z|^2 + |u_y|^2) dV / \int_{V_{\text{unitcell}}} (|u_z|^2 + |u_y|^2) dV$ where u_y and u_z are the main components of the displacement field. The result of the band sorting calculation is presented in Figs. 12(c) and 12(d) using a grayscale color bar.

Now, in the transmission spectrum, only the leaky modes at $k_x = 0$ can be observed because the incident wave is launched normal to the rows of holes (i.e., with $k_x = 0$). However, the selective peaks in the transmission can be related only to those modes which are induced by the holes and, therefore, have a sufficient localization in their near vicinity. This means that some of these modes can result from the penetration into the leaky region of the nonleaky branches situated below the sound line as illustrated in Fig. 12(c), where modes in the leaky region defined by red font S_1, S_2, S_3, and A_1 and their continuation in nonleaky region by black font. The mentioned phenomenon is observed for both S and AS modes. However the situation gets complicated at the high frequency range starting from 2500 m/s.

To make the connection between the frequencies of the peaks in the transmission and the modes at $k_x = 0$ in the band structure, we give Figs. 13(a) and 13(b) the dispersion curves with band sorting calculated for the case $w = 0.4a$. The displacement fields associated with the points A_1, A_2, S_1, and S_3 are represented Fig. 13(c). The mode S_2 is not excited due to the symmetry reasons. One can easily recognize the similarity between these maps and those given in Fig. 6 for symmetric and in Fig. 11 for antisymmetric modes.

IV. PHONONIC CRYSTAL

We report in this section the evolution of the transmission of S_0 modes and the larger low frequency band gap of the band gap when increasing the number of rows constituting the phononic crystal for a constant set of geometrical parameters i.e., $l = 0.4a$, $d = 0.9a$, and $w = 0.35a$. Figure 14(a) shows the respective band structure for a phononic crystal in the ΓX direction which contains symmetric and antisymmetric waves and shear horizontal (SH) waves colored in red, black, and blue respectively. One can remark the formation of a band gap for all types of modes in the range $2000 < fa < 3000$ m/s. The formation of the band gap is shown in Fig. 14(b) for the S_0 modes by adding progressively the numbers of rows of holes ($N = 2,3,$and 4). In the transmitted frequency bands ($fa <$ 1000 and $fa >$ 3000 m/s) the number of peaks increases in agreement with the number of horizontal bars of the H element, constituting progressively Fabry-Perot oscillations between the horizontal bars. Between the two transmitted bands, a first band gap is constituted with attenuation over 10^{-3} as compared to the input signal (in the region of fa from 1660 to 2830 m/s). We stress that this wide low frequency band gap finds its origin in the fundamental eigenmodes of the H-element.

V. CONCLUSIONS

In conclusion, we have investigated the transmission of symmetric Lamb waves propagating through a thin silicon plate drilled with one or two rows of rectangular air holes. In both cases, we found the existence at high frequency of specific peaks and a dip which correspond to the coupling of the incident wave with both Fabry-Perot oscillations inside the vertical junctions and induced interface waves between the homogeneous media and the row of holes. When adding a second row of holes, we show the occurrence of low frequency modes which have been associated to eigenmodes localized inside the horizontal bar of an H element. With an appropriate choice of the distance between the two holes, we have shown that the structured plate behaves like an acoustic metamaterial displaying a wide subwavelength band gap for symmetric and antisymmetric Lamb waves under normal stress with

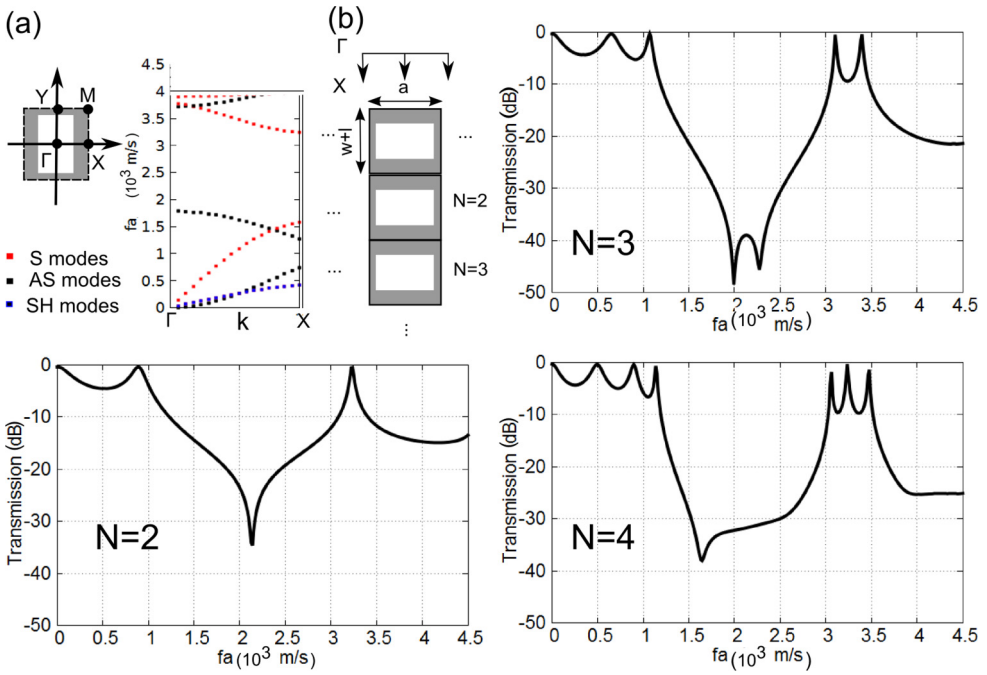

FIG. 14. (Color online) (a) Elementary unit cell of the phononic crystal with periodic conditions applied in the x and y directions. Band structure of the phononic crystal in ΓX direction for the modes symmetric (red), antisymmetric (black), and shear horizontal (blue) for the geometrical parameters $w = 0.35a$ and $l = 0.4a$. (b) Overview of the low frequency gap formation ($fa < 3000$ m/s) from the transmission curves for an increasing number of unit cells for the symmetric Lamb modes.

an attenuation over 99% for the symmetric waves at a wide low frequency range and over 90% for antisymmetric waves. By increasing the length of the holes we introduce sharp Fabry-Perot resonances peaks in the gap region which open the way to filtering and sensing applications. We have shown that the finite slab drilled with rectangular air holes cover the important domains of the acoustic metamaterials topic and can find many applications in the field of a low frequency band gap. This subwavelengths investigation should have implications for sound isolation, imaging, and sensing applications.

ACKNOWLEDGMENTS

The work is supported by the Agence Nationale de la Recherche (ANR) and Direction Générale de l'Armement (DGA) under the project Metactif, Grant No. ANR-11-ASTR-0015.

[1] M. S. Kushwaha, P. Halevi, L. Dobrzynski, and B. Djafari-Rouhani, Phys. Rev. Lett. **71**, 2022 (1993).
[2] M. M. Sigalas and E. N. Economou, Solid State Commun. **86**, 141 (1993).
[3] Y. Pennec, J. Vasseur, B. Djafari-Rouhani, L. Dobrzynski, and P. Deymier, Surf. Sci. Rep. **65**, 229 (2010).
[4] J. Bucay, E. Roussel, J. O. Vasseur, P. A. Deymier, A.-C. Hladky-Hennion, Y. Pennec, K. Muralidharan, B. Djafari-Rouhani, and B. Dubus, Phys. Rev. B **79**, 214305 (2009).
[5] Z. Liu, X. Zhang, Y. Mao, Y. Y. Zhu, Z. Yang, C. T. Chan, and P. Sheng, Science **289**, 1734 (2000).
[6] L. Fok, M. Ambati, and Z. Xiang, MRS Bull. **33**, 931 (2008).
[7] Y. Pennec, B. Djafari-Rouhani, H. Larabi, J. O. Vasseur, and A. C. Hladky-Hennion, Phys. Rev. B **78**, 104105 (2008).
[8] T.-T. Wu, Z.-G. Huang, T.-C. Tsai, and T.-C. Wu, Appl. Phys. Lett. **93**, 111902 (2008).
[9] Y. Pennec, B. Djafari Rouhani, H. Larabi, A. Akjouj, J. N. Gillet, J. O. Vasseur, and G. Thabet, Phys. Rev. B **80**, 144302 (2009).
[10] M. Badreddine Assouar and M. Oudich, Appl. Phys. Lett. **100**, 123506 (2012).
[11] J.-C. Hsu, J. Phys. D: Appl. Phys. **44**, 055401 (2011).
[12] J. Christensen, L. Martin-Moreno, and F. J. Garcia-Vidal, Phys. Rev. Lett. **101**, 014301 (2008).
[13] M.-H. Lu, X.-K. Liu, L. Feng, J. Li, C.-P. Huang, Y.-F. Chen, Y.-Y. Zhu, S.-N. Zhu, and N.-B. Ming, Phys. Rev. Lett. **99**, 174301 (2007).
[14] X. Zhang, Phys. Rev. B **71**, 241102 (2005).
[15] Y. Li, B. Liang, X.-y. Zou, and J.-c. Cheng, Appl. Phys. Lett. **103**, 063509 (2013).
[16] Z. He, S. Peng, R. Hao, C. Qiu, M. Ke, J. Mei, and Z. Liu, Appl. Phys. Lett. **100**, 091904 (2012).
[17] H. Estrada, F. J. García de Abajo, P. Candelas, A. Uris, F. Belmar, and F. Meseguer, Phys. Rev. Lett. **102**, 144301 (2009).
[18] Z. Liu and G. Jin, J. Phys.: Condens. Matter **22**, 305003 (2010).
[19] F. Liu, M. Ke, A. Zhang, W. Wen, J. Shi, Z. Liu, and P. Sheng, Phys. Rev. E **82**, 026601 (2010).
[20] A. Santillán and S. I. Bozhevolnyi, Phys. Rev. B **84**, 064304 (2011).

[21] J. Sánchez-Dehesa, D. Torrent, and L.-W. Cai, New J. Phys. **11**, 013039 (2009).
[22] H. Jia, M. Ke, C. Li, C. Qiu, and Z. Liu, Appl. Phys. Lett. **102**, 153508 (2013).
[23] Z. He, H. Jia, C. Qiu, S. Peng, X. Mei, F. Cai, P. Peng, M. Ke, and Z. Liu, Phys. Rev. Lett. **105**, 074301 (2010).
[24] S. Peng, C. Qiu, Z. He, Y. Ye, S. Xu, K. Tang, M. Ke, and Z. Liu, J. Appl. Phys. **110**, 014509 (2011).
[25] Z. Yang, H. M. Dai, N. H. Chan, G. C. Ma, and P. Sheng, Appl. Phys. Lett. **96**, 041906 (2010).
[26] A. Elayouch, M. Addouche, E. Herth, and A. Khelif, Appl. Phys. Lett. **103**, 083504 (2013).
[27] H. Estrada, P. Candelas, A. Uris, F. Belmar, F. J. García de Abajo, and F. Meseguer, Phys. Rev. Lett. **101**, 084302 (2008).
[28] R. Hao, C. Qiu, Y. Ye, C. Li, H. Jia, M. Ke, and Z. Liu, Appl. Phys. Lett. **101**, 021910 (2012).
[29] Z. He, H. Jia, C. Qiu, Y. Ye, R. Hao, M. Ke, and Z. Liu, Phys. Rev. B **83**, 132101 (2011).
[30] H. Estrada, P. Candelas, F. Belmar, A. Uris, F. J. García de Abajo, and F. Meseguer, Phys. Rev. B **85**, 174301 (2012).
[31] Y. Pennec, B. D. Rouhani, H. Larabi, A. Akjouj, and G. Lévêque, New J. Phys. **14**, 073039 (2012).
[32] R. W. Wood, Proc. Phys. Soc. London **18**, 269 (1902).
[33] R. W. Wood, Phys. Rev. **48**, 928 (1935).
[34] D. Royer and E. Dieulesaint, *Elastic Waves in Solids* (Wiley, New York, 1999).
[35] Comsol Multiphysics, Structural Mechanics Module, User's Guide, Version 4.1, http://www.comsol.com/ (2010).